LUNG DAMAGE

LUNG DAMAGE

A CAD system for detection of lung damage

Jens Tranholm Olesen
Spring 2012 - 12gr1080

AALBORG UNIVERSITY

Department of Health Science and Technology
www.hst.aau.dk

Title:
A CAD system for detection of lung damage

Subject:
Medical Informatics

Project period:
P10, spring semester 2012
February 1st – June 4th 2012

Project group: 12gr1080

Author:

Jens Tranholm Olesen

Supervisors:
Lasse Riis Østergaard
Anne Sofie Korsager

Worksheets page count: 49

ABSTRACT:

CAD systems are increasingly relied on for the identification and quantification of lung damage following radiation therapy. However the ability to classify several types of lung damage using the same features and classifier is often difficult. As a part of this work, the use of different subvolume sizes was examined, showing that larger volumes provide better classification. The use of sub volumes of size 21x21x21 to distinct between treated non-pneumonitis tissue and treated pneumonitis tissue, was found to produce an accuracy of 88.7%. However, future work should focus on including the counter lateral lungs in the classification.

Preface

This project is made by Jens Tranholm Olesen (12gr1080) on the 10th semester of Biomedical Engineering and Informatics at Aalborg University.

Acknowledgements

The author would like to express his greatest gratitude for the help and support given by:

- Jesper Carl, Chief Physicist

and the rest of the staff at the Department of Medical Physics, Aalborg Hospital, Aarhus University. A special thanks also goes to Lasse Riis Østergaard and Anne Sofie Korsager at Aalborg University for supervising the project and arranging the contact with Aalborg Hospital.

Literature

A literature search was conducted at the very beginning of the project. The methodology behind is described in Appendix A.
References to literature are made using the Harvard method, in which the authors last name and the year of publishing is placed in brackets, [Last name, Year]. When an in-text reference is given, the source can subsequently be found in the list of references (page 38), where all sources are listed in alphabetical order.

Figures and tables

Figures and tables are numbered sequentially according to their appearance in the text and the chapter in which they are placed. For example, a figure numbered as 3.2, is the second figure in chapter 3. A description of the figure or table contents is located below the object along with a reference to the source. If no source is given, the figure or table belongs to the author of this report.

Contents

CHAPTER 1

Introduction

It is probably no surprise that lung cancer is the most common type of cancer in the world, also when judging by both incidence and mortality rates. Statistics from the World Health Organization (WHO) show that by 2008 an estimated 1.61 million new cases were seen each year and a reported 1.38 million deaths [Ferlay et al., 2010]. Generally, lung cancer has shown little improvement in survival rate over time, despite improvements in diagnosis and treatment, making it evident that continued research is needed within the field [Siegel et al., 2012].

A specific area of interest for researchers are the adverse effects of radiation therapy, which in combination with chemotherapy, is the treatment of choice for advanced non-small-cell lung cancer (NSCLC) [E. Lim et al., 2010]. An estimated 1- 20% of patients undergoing radiotherapy or chemoradiotherapy, develop moderate to severe radiation pneumonitis (RP) within the first few weeks [Marks et al., 2003; Mehta, 2005; Rovirosa & Valduvieco, 2010]. According to Rodrigues et al. [2004], the number should be even higher, with an incidence rate around 13-37%. However, the incidence rates prove difficult to determine precisely, as discussed by Kocak et al. [2005] and Yirmibesoglu et al. [2012]. The latter recently conducted a large retrospective review of 434 irradiated patients and concluded that within the 17% who were diagnosed as affected by RP, a 48% diagnostic uncertainty existed.

The uncertainty arises due to the relatively limited clinical syndromes of pneumonitis, which are defined as mild dyspnea, non-productive mild cough, low-grade fever and pleuritic chest pain, making physical examination and laboratory findings unreliable [Berkey, 2010; Rovirosa & Valduvieco, 2010]. As a consequence of this, clinicians have started utilizing computer-assisted-detection (CAD) systems to identify pneumonitis and other lung diceases within medical images of the lungs and correlate the radiographic findings with the underlying pathology and syndromes [Fass, 2008; Shiraishi et al., 2011].

In order for the CAD systems to provide a reliable evaluation, they must be able to detect and distinct between altered attenuations, as well as nodular, reticular or linear abnormalities, which may occur alone or mixed together in the images. Damage caused by pneumonitis has so far proven difficult to detect, due to its diffuse and hazy appearance in medical images [Provatopoulou et al., 2008]. This has lead to the development of several distinct algorithms for analysis,

among which the newest use wavelet filtering, fuzzy k-nearet neighbor, Markov random fields, support vector machines or artificial neural networks [Gangeh et al., 2011; Palma et al., 2011; Park et al., 2011; Tolouee et al., 2011; Zhu et al., 2011]. Common for all, is the evaluation of lung tissue texture, which is complicated by the interference of pulmonary and air tree vessels.

1.1 Aim

The purpose of this study is to develop an algorithm which is able to detect radiation-induced pneumonitis within follow-up CT studies of patients undergoing radiation therapy.

PART

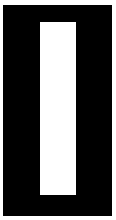

Background

CHAPTER 2

Radiation-induced pneumonitis

Due to its extremely radiosensitive tissue, the lungs are prone to radiation-induced injuries to the normal lung parenchyma surrounding the target of radiation, e.g. neoplasm. The damage occurs when energy generated by the radiation, is released. This generates free radicals, which are believed to cause macromolecular cell damage and DNA alterations [Ataya et al., 2006]. The result of this, is an activation of inflammatory processes which become self sustained once established, due to the vast amounts and distinctive damages generated during irradiation [Provatopoulou et al., 2008].

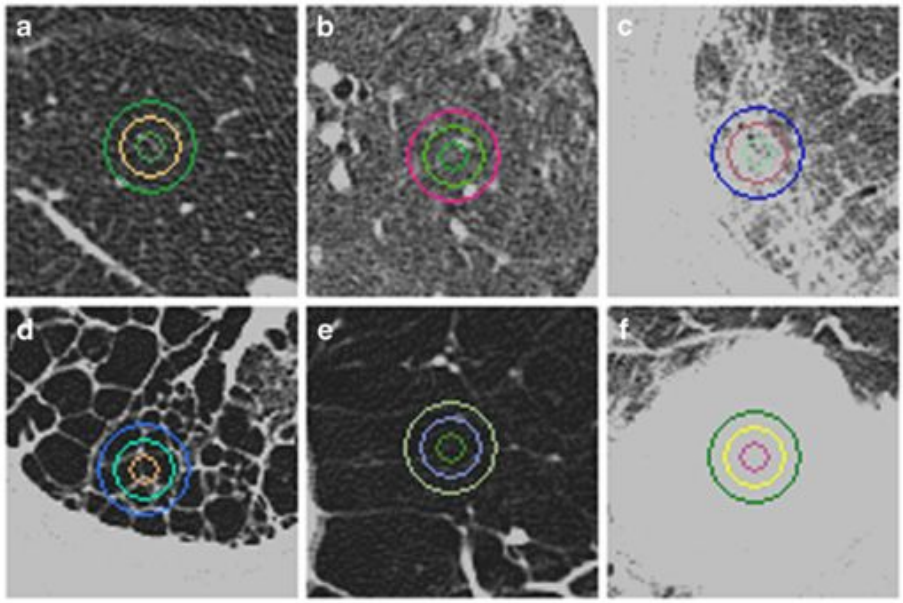

Figure 2.1: *A example of types of lung damage. a normal, b ground-glass opacity, c reticular opacity, d honeycombing, e emphysema, f consolidation [J. Lim et al., 2011]*

Both X-ray and CT are utilized in order to monitor the possible development of pneumonitis, which develops as a diffuse haze and later becomes more consolidated within the area of the treatment portals [Provatopoulou et al., 2008]. The findings are typically divided into six different types, called honeycombing, emphysema, reticular opacities, ground-glass opacities and consolidation, as seen on figure 2.1.

Studies have shown that 50% to 90% of the patients that receive ra-

diotherapy in the chest area, develop abnormalities in either the pulmonary function or the lung parenchyma [Rovirosa & Valduvieco, 2010]. It is therefore a key interest of physicians to efficiently monitor the development of pneumonitis and compare it to the amount of radiation therapy administered [Bagci et al., 2012].

2.1 Computer-aided diagnosis systems

CAD systems are increasingly used to detect abnormalities such as pneumonitis, in order to reduce the time consuming process of visually inspecting the large image sets, as well as quantifying the amount of damage. These systems utilize various methods of texture analysis, such as the low-level features produced by Gray-level Co-occurrence matrices and general shape features computed using binary transforms of image subvolumes [Bagci et al., 2012]. A large portion of the possible features used to detect lung damage is shown in figure 2.2

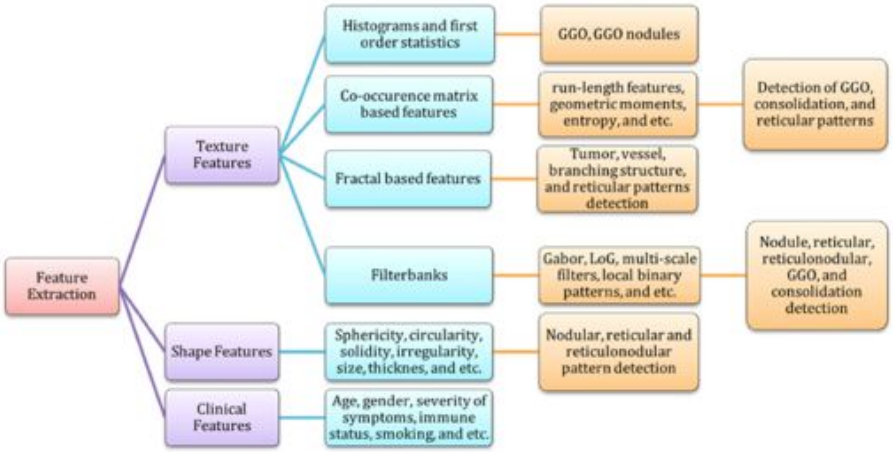

Figure 2.2: *Types of features used in CAD systems for detection of lung damages [Bagci et al., 2012]*

The systems are generally comprised of the three main routines: data acquisition, segmentation of region and texture analysis, after which the features are fed to a classifier. (see figure 2.3).

Examples of the different classification algorithm used for lung damage identification, are shown in table A.1. As seen, the CAD systems usually focus on a specific type of pneumonitis, due to the vast textural differences.

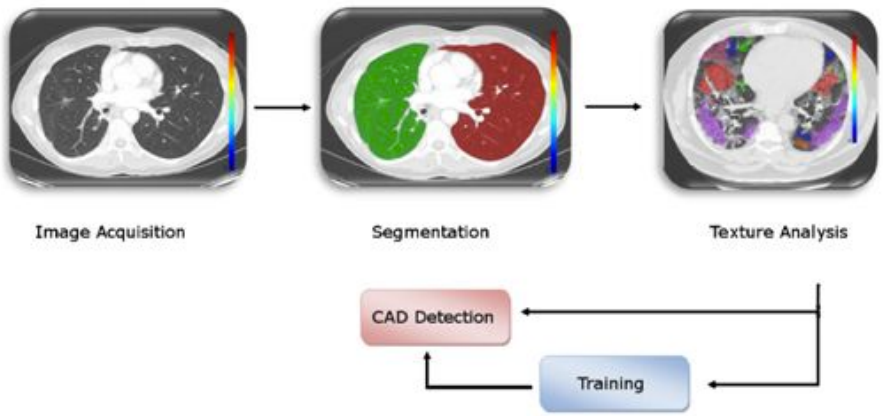

Figure 2.3: *The build-up of a CAD system [Bagci et al., 2012]*

Study	Algorithm	Disease categories	Data	Comparison	Performance
Zhu et al. [2011]	Markov random field-based.	Ground-grass opacity.	41 subjects	First compared to gold standard created by three radiologists. Segmentations were then examined by 2 radiologists.	Sensitivity: 86.94% Specificity: 94.33% Accuracy: 94.06%
Tolouee et al. [2011]	Wavelet filtering. Fuzzy k-nearest neighbor.	Normal Honeycombing. Ground-glass opacity. Reticular opacities.	17 subjects 399 images	Compared with two state-of-the-art texture based methods and examinations by two radiologists.	Avg. Sensitivity: 91.33% Avg. Specificity: 96.94% Avg. Accuracy: 95.91%
Gangeh et al. [2011]	Support vector machines.	Emphysema.	168 ROIs	Compared to annotated ROIs and two other techniques	Accuracy: 95.00%
Palma et al. [2011]	B-spline-based. Deformable registration.	Pneumonitis. Fibrosis.	25 subjects	Relationship between lung density and clinician-scored radiological pneumonitis was compared.	Lung density around tumor correlated with increased severity of radiological pneumonitis (Spearman's r=0.75; p<0.001).
Park et al. [2011]	Artificial neural network	Normal. Interstitial lung disease.	38 subjects	Comparison made between normal and ILD subjects	AUC: 0.884 ± 0.064 Sensitivity: 80.00 % Specificity: 87.70%

Table 2.1: *Previous studies within computer-assisted detection of lung diseases.*

PART II

Method

CHAPTER 3

Development approach

A CAD system was developed for the purpose of detecting occurrences of pneumonitis tissue from subjects who have undergone radiation therapy. The idea is to first segment the lungs of each subject and then extract subvolumes needed to perform the texture analysis. The analysis was performed using the features of Haralick, which are calculated on Gray-Level Co-orcurrence Matrices (GLCM). Finally, a subset of the features were used to optimize and train a Support Vector Machine (SVM), while a separate subset was used for the classification.

3.1 Data collection

CT studies of six subjects, taken three months after finishing their therapy sessions, were obtained from the Department of Oncology at Aalborg Hospital, which provide the radiation therapy to lung cancer patients. The studies were chosen by an experienced radiologist who classified four of the subjects as having pneumonitis (RP_{pos}), while two were without (RP_{neg}). Each RP_{pos} subject was characterized by having a more dominant type of pneumonitis within the lungs, e.g. ground-glass opacity, consolidation, reticular opacities, micro nodules or honeycombing. One RP_{neg} subject was removed due to its reduced lung size caused by lung damage, making extraction of sub volumes impossible.

All scans were captured using helical CT with a resolution of 512 x 512 pixels and a beam energy of 120 kVp. For a more detailed description of the data used see Table 3.1.

The health information stored within the DICOM-RT headers were immediately anonymized in accordance with clinical guidelines, after which the data was imported into MatLab using the Computational Environment for Radiotherapy Research (CERR). The CERR application automatically makes the data uniform.

3.2 Examples

As shown in figure 3.1, four of the subjects (RP_{pos}) have diagnosed signs of pneumonitis, while the remaining two (RP_{neg}) only contain remains of the shrinking lung nodules/tumor.

Ref. subject	**No. slices**	**Avg. Tube current** [mA]	**Pixel spacing** [mm]	**Slice thickness** [mm]	**Class type**
5	135	211	0.7578	5	RP_{pos}
6	83	186	0.6309	5	RP_{pos}
7	60	-	0.7773	5	RP_{pos}
8	84	178	0.6367	5	RP_{pos}
9	141	276	0.7813	3	RP_{pos}
22	76	375	0.7422	6	RP_{neg}
37	246	173	0.8203	2.5	RP_{neg}

Table 3.1: *Overview of data used to develop and test the algorithm. The average tube current for subject no. 7 was not present in the header information.*

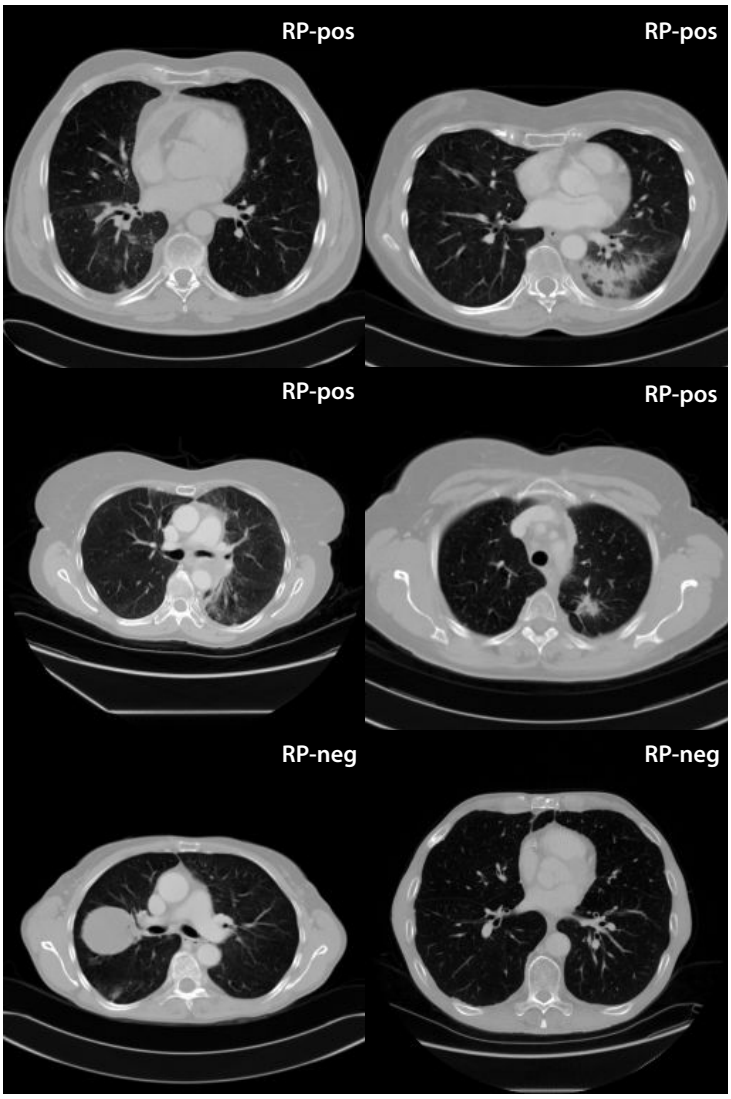

Figure 3.1: *A slice from each subject depicting the severity of injuries.*

CHAPTER 4

Lung segmentation

The following sections focusses on the method of which the right and left lung were segmented in order to provide a boundary for the texture analysis. The segmentation was done using wavefront propagation after which the segmented regions were processed using morphological hole filling. Afterwards, the obtained regions are filled with different sized consecutive subvolumes within the lungs.

4.1 Wavefront propagation

The algorithm was used to segment three different areas of the torso. First the airway tree from trachea to the bronchial bifurcation was segmented in order to subtract it from the regions of the lung. A seed point was placed within the trachea, after which the wavefront was allowed to propagate. Every time a bifurcation was encountered, the wavefront would split and form two new fronts.

The specific implementation of the propagation technique which was used in this work, contains a priority-queuing system which maximizes the performance of the propagation algorithm. Following the initiation of a wavefront segment from a seed point, the segments connected to the perimeter of the segment are added to a queue, as described on figure 4.2. The list is a "First-in, first-out" list, which ensures that branches from upper areas of the lung are segmented first. Following the propagation of a wavefront, the front is evaluated to assess whether leakage has occurred. This is typically done by comparing the surface area of the new wavefront, with the previous. A large difference between these values indicate that the surrounding borders have been breached by the wavefront, after which the threshold for wavefront edge pixel intensities is raised. Another interesting feature of the algorithm is the ability to compare the segment that the wavefront is propagating from, by evaluating the size of the diameter for the previous and current segment. This is a vital function when segmenting tree structures like the airway tree.

During the validation of the new propagation and segment, the children of the wavefront are either added to the queue or removed, after which the next segment in queue is processed instead.

In addition to the use of the algorithm for segmentation of the airway

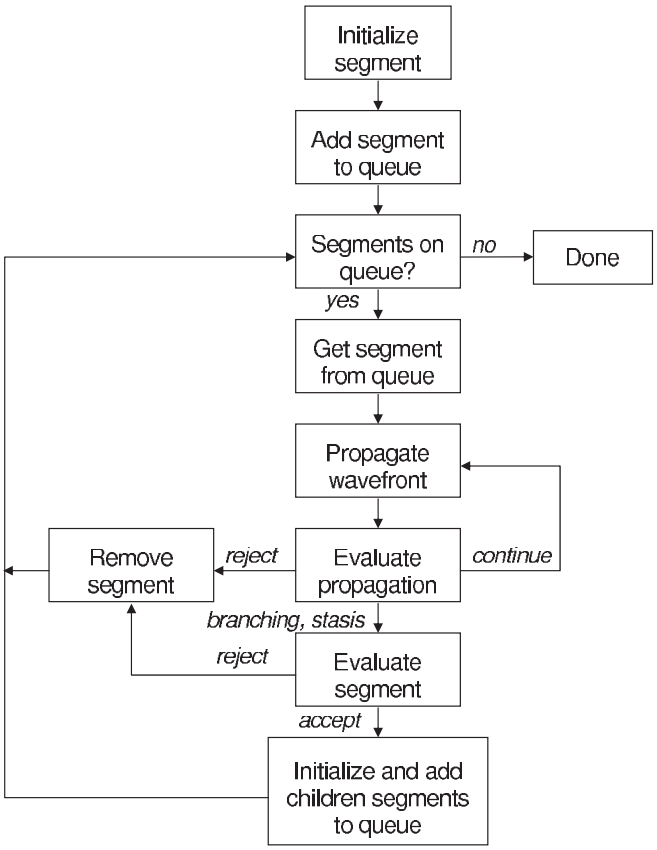

Figure 4.1: *Diagram of the steps involved in wavefront propagation [Artaechevarria et al., 2009].*

tree, the wavefront propagation can also be applied to the segmentation of the individual lungs. This was done by lowering the rules, thereby allowing the wavefront to propagate in spite of a large differences between the previous and new wavefront, which would occur within the large regions of the lungs. The result of this is a finely segmented lung region from which the airway tree is subtracted in order to remove the segments that have propagated from the lungs and back upwards through the trachea.

Thereafter, the holes in the segmented region is removed using morphological hole filling, as shown in figure 4.2.

4.2 Extraction of subvolumes

The solid lung regions were then used as the boundary for the filling of subvolumes within each lung, as depicted in figure . Firstly, the subvolumes are positioned within the lung in a manner which maximizes the amount, after which the intensity values of the original image are isolated within each subvolume area. Subvolumes of size (13x13x13, 17x17x17 and 21x21x21) are extracted from each subject.

Original Wavefront Propagation Hole filling

Figure 4.2: *Example showing the segmentation of a right lung from an original dicom image, using wavefront propagation and hole filling.*

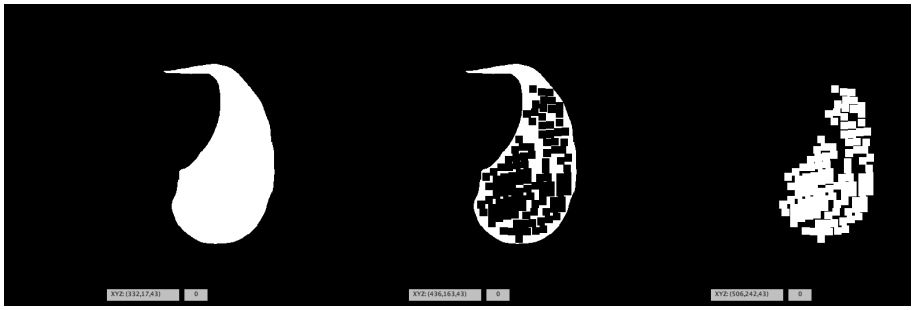

Segmentation Voxel positioning Voxel extraction

Figure 4.3: *Example showing the steps involved in extracting subvolumes from a segmentation by first positioning the subvolumes areas and then isolating the original intensity values within the individual subvolumes.*

CHAPTER 5

Texture analysis

The texture analysis was performed using 3D GLCMs on the subvolumes obtained from each group of subjects. In this work, the method was combined with a support vector machine classifier.

5.1 Gray-level co-occurance matrices

The GLCM called $Co(i, j)$ provides a measurement of how often a gray-scale pixel i occurs adjacent to pixels with the value j, in either or all of the four 2D directions (0°, 45°, 90°, 135°). In addition to the direction, it is also possible to choose the distance between the pixel of interest i and the neighbor j, allowing for multiple calculations.

A simple example of the calculation is presented in figure 5.1. The image I to the left is being analyzed in order to create the GLCM Co to the right. One neighboring pixel pair of ones are placed in $Co(1,1)$, while the two pairs for ones next to twos, are counted and placed in $Co(1,2)$, since the pixel of interest is 1 [Sebastian et al., 2012].

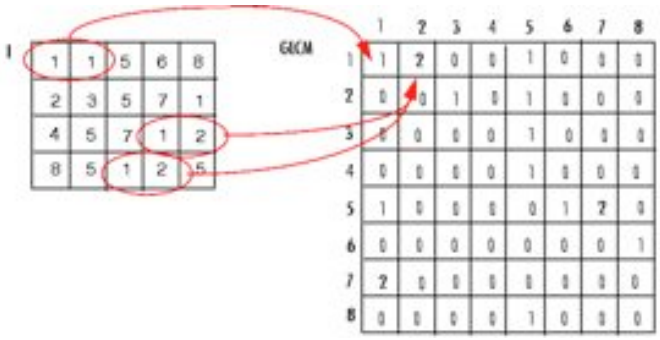

Figure 5.1: *Simple example of the transformation of an image I to an GLCM $Co(i, j)$ [MathWorks Inc.].*

However, the difference with the 3D GLCM, is the additional 9 directions that can be calculated, making the GLCM multidimensional itself.

5.2 Features

Following the construction of the GLCM, a variety of different features are calculated based on the values of $Co(i, j)$. The features used

are the famous Haralick features.

$f_{Energy} = \sum_{i=1}^{N} \sum_{j=1}^{N} Co^2(i,j)$

$f_{Entropy} = -\sum_{i=1}^{N} \sum_{j=1}^{N} Co(i,j)\ log_{10}(Co(i,j))$

$f_{Correlation} = \frac{1}{\sigma_x \sigma_y} \sum_{i=1}^{N} \sum_{j=1}^{N} (i\ j)\ Co(i,j) - \mu_x \mu_y$

$f_{Contrast} = \frac{1}{(N-1)^2} \sum_{i=1}^{N} \sum_{j=1}^{N} (i-j)^2\ Co(i,j)$

$f_{Homogeneity} = \sum_{i=1}^{N} \sum_{j=1}^{N} \frac{1}{1+(i-j)^2}\ Co(i,j)$

$f_{Variance} = \sum_{i=1}^{N} \sum_{j=1}^{N} (i-\mu)^2\ Co(i,j)$

$f_{Sum\ mean} = \sum_{i=2}^{2N} i\ Co_{x+y}(i)$

$f_{Inverse\ difference\ moment} = \sum_{i=1}^{N} \sum_{j=1}^{N} \frac{Co(i,j)}{|i-j|^2}\ ij$

$f_{Cluster\ shade} = \sum_{i,j=1}^{N} (i - \sum_{i,j=1}^{N} i\ Co(i,j) + j - \sum_{i,j=1}^{N} j\ Co(i,j))^4\ Co(i,j)$

$f_{Cluster\ tendency} = \sum_{i,j}^{N} (i - \sum_{i,j=1}^{N} i\ Co(i,j) + j - \sum_{i,j=1}^{N} j\ Co(i,j))^4\ Co(i,j)$

$f_{Max\ probability} = Max\left[Co(i,j)\right]$

Using separability and correlation analysis (SEPCOR) the sum mean and cluster prominence were found to be the most descriptive features.

PART III

Validation

CHAPTER 6

Validation of lung segmentation

In order to extract subvolumes of size 13x13x13, 17x17x17 and 21x21x21 within the lungs, it was necessary to segment each lung and afterwards fill the generated binary mask with as many subvolumes as possible. The qualitative results of the segmentation and extraction of subvolumes from each subject is presented in the following.

6.1 Method

Since there is no ground truth segmentation for the datasets provided by the hospital, a qualitative evaluation of the segmentation obtained using wavefront propagation, is performed instead on all subjects.

The segmentations were done using the parameters for wavefront propagation presented in table 6.1.

Location	**Variable**	**Value**
Airway		
	Image threshold	–820 HU
	Maximum difference	180
	Voxel limit	4.000.000
Lungs		
	Image threshold	-500 HU to -300 HU
	Maximum difference	500-700
	Voxel limit	6.000.000
Default for both		
	Wavefront expansion ratio	1.1
	Segment expansion ratio	1.1
	Connectivity	18

Table 6.1: *Variable values used during validation of lung field segmentation.*

For each subject a seed point was placed within the trachea and each of the lungs. All seed points were placed in areas with a low intensity, allowing the wavefront propagation algorithm to function properly.

6.2 Results

The obtained segmentation of each lung in each subject is presented in figure 6.1-6.6, while a 3D view of the extracted subvolumes from subject 5 is shown in figure 6.7-6.8.

Figure 6.1: *Subject 5: Result of segmentation*

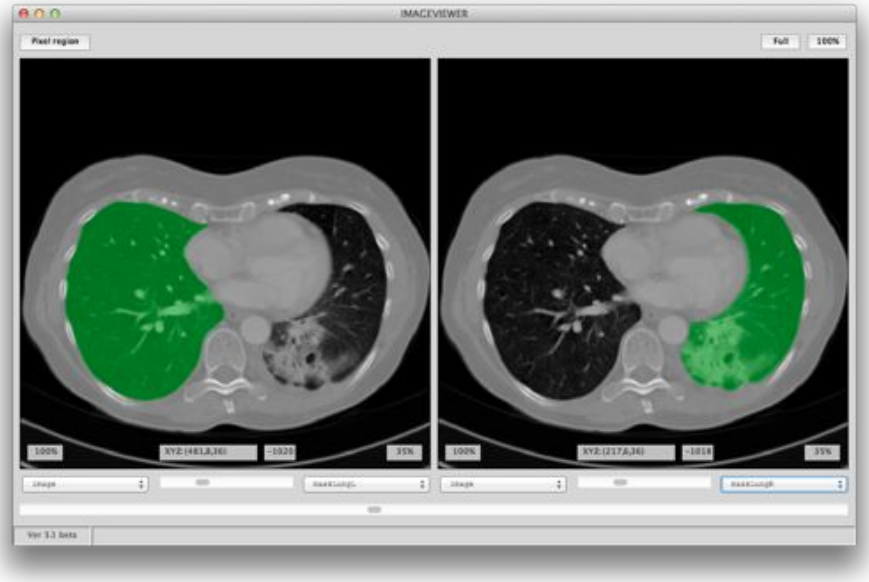

Figure 6.2: *Subject 6: Result of segmentation*

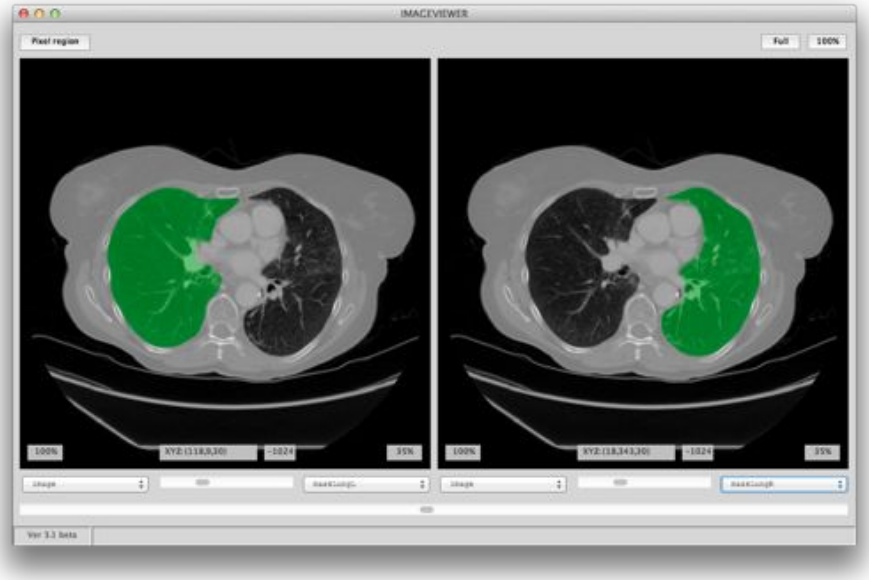

Figure 6.3: *Subject 7: Result of segmentation*

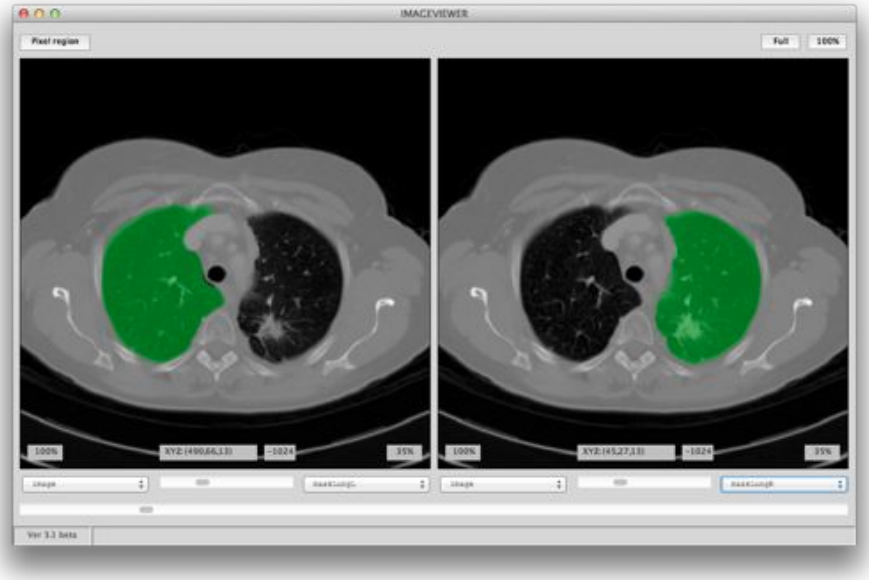

Figure 6.4: *Subject 8: Result of segmentation*

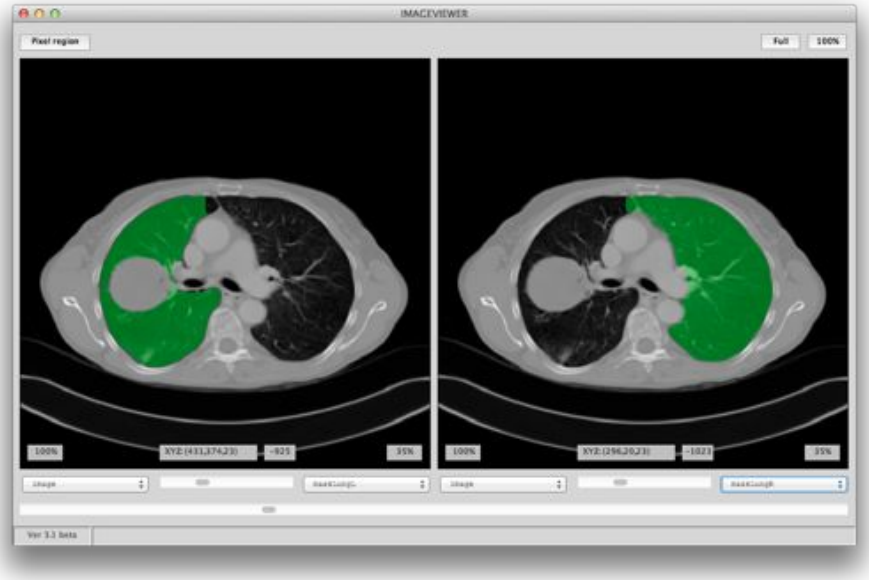

Figure 6.5: *Subject 22: Result of segmentation*

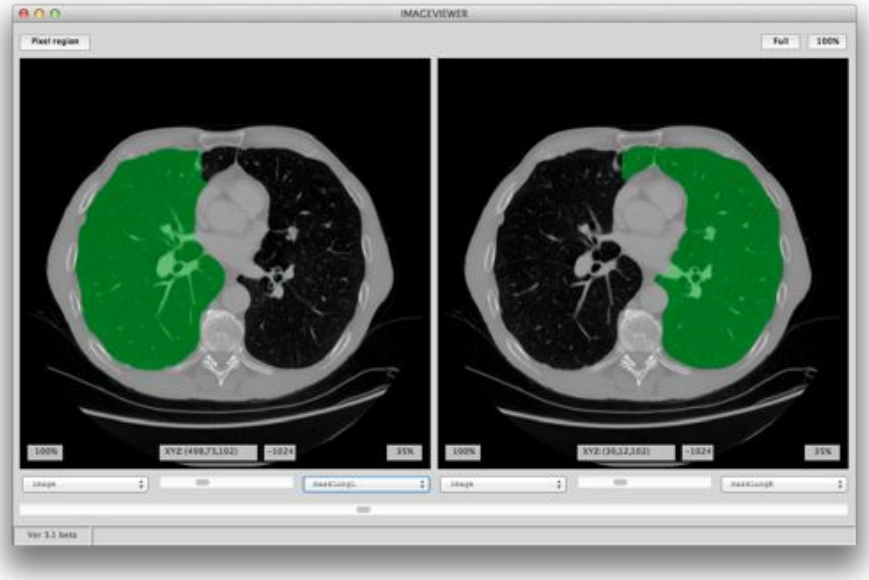

Figure 6.6: *Subject 37: Result of segmentation*

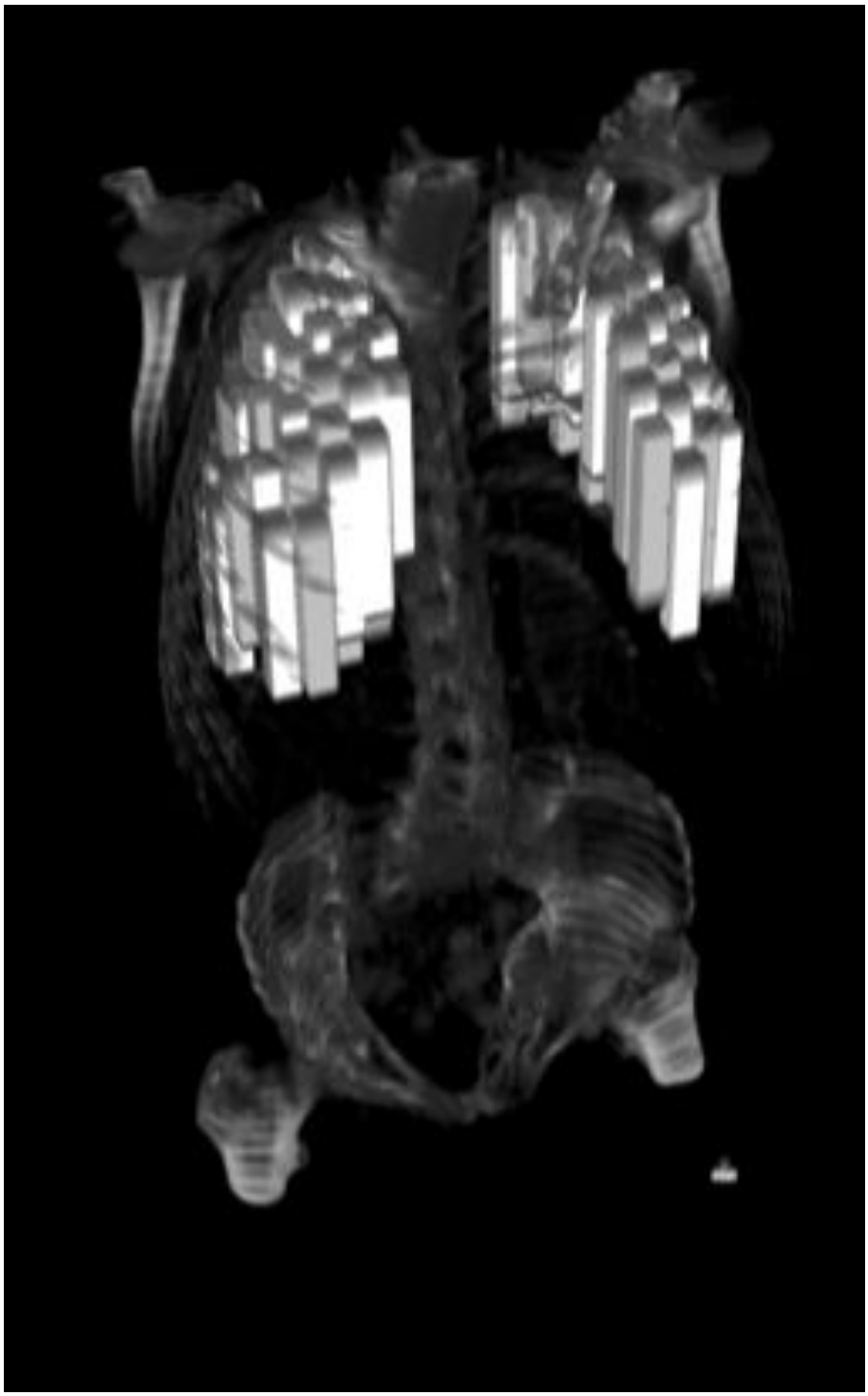

Figure 6.7: *3D view of subvolumes extracted from subject no. 5. Due to the interpolation, the individual subvolumes are visually combined in the image, even though the are separate entities.*

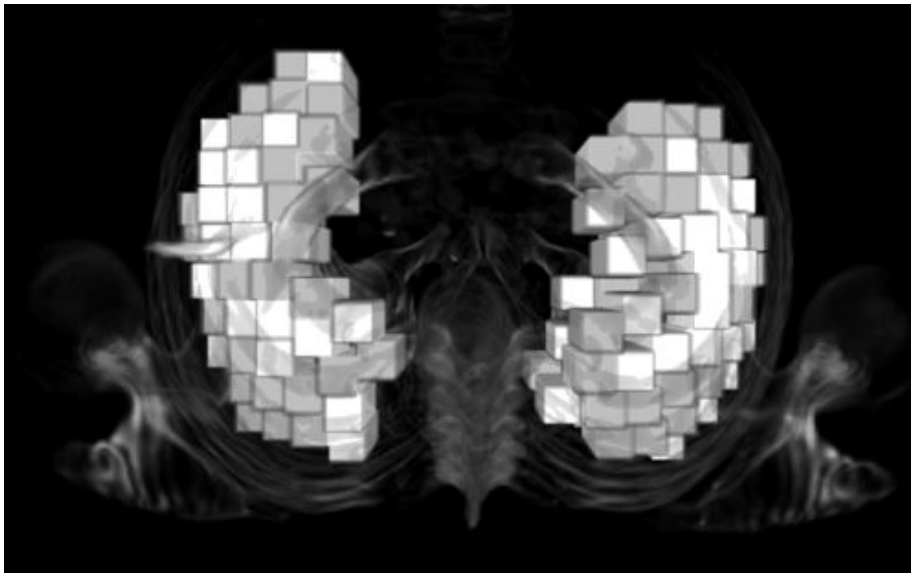

Figure 6.8: *Top to bottom 3D view of subvolumes extracted within the lungs of subject no. 5*

6.3 Discussion

The lung regions (including pulmonary vessels and airway tree elements within the lung itself) were successfully segmented in subject 5-9, while subjects 22-37 contained a thin and weakly contrasted junction line between the two lungs, allowing the wavefront to propagate into the neighboring lung region. This is the result of a tradeoff between the degree of segmentation of pneumonitis areas and separability of large regions. With regards to subject 22, the left lung contained a large tumor which the algorithm avoided as intended.

Following the lung segmentation, the subvolumes of size 13x13x13, 17x17x17 and 21x21x21 within the lungs, were extracted. This was performed with success, as seen in the example in figure 6.7-6.8.

It is worth noting that all lung segmentations contain both pulmonary and airway vessels in addition to the parenchyma. This could have been avoided by segmenting the whole airway tree and pulmonary vessel tree and subtracting them from the lung segmentation. However, the relatively large slice thickness made it impossible for the wavefront propagation algorithm to move into smaller lung nodes. Also, the subtraction of non-parenchyma objects would have lead to a significant reduction in the number of subvolumes that could be extracted from within the segmented regions.

CHAPTER 7

Validation of texture analysis

In order to detect areas with pneumonitis, the extracted subvolumes from both groups of subjects, were analyzed using GLCM and classified using a SVM. The division of data, optimization and training of the classifier, as well as the texture classification itself, is presented in the following.

7.1 Method

Data was divided into a training and test set, with 60% being training subvolumes and 40% being test subvolumes. Both sets contain as equal amounts of both RP_{neg} and RP_{pos} as possible. With regards to the RP_{pos} subjects, only the subvolumes from the irradiated (area receiving above 50% of the dose) lung in which the pneumonitis was present, was used. On the other hand, both lungs from the RP_{neg} subjects were used, giving four lungs classified as having pneumonitis and four without. The use of both the irradiated and non-irradiated lung from the RP_{neg} subjects, was due to slight remains of tumor tissue, which resembles pneumonitis. The opposite lung would function as a balance to this.

The division of the data for each subvolume size is presented in table 7.1.

subvolume size	**13 x 13 x 13**	**17 x 17 x 17**	**21 x 21 x 21**
Total subvolumes	3380	1304	597
Train subvolumes RP_{neg}	1524	600	287
Train subvolumes RP_{pos}	504	183	72
Test subvolumes RP_{neg}	1016	399	190
Test subvolumes RP_{pos}	336	122	48

Table 7.1: *The amount of subvolumes extracted totally and for each group.*

Prior to the classification of data, the SVM classifier is trained using the training set. However, an unconstrained nonlinear optimization combined with a five-fold cross-validation was first performed in order to optimize the training process. The purpose of the grid search was to estimate the value sigma of the gaussian radial basis function used as the kernel, as well as the box constraint. The sigma value rep-

resents the scaling or width of the gaussian function, while the box constraint controls the soft margin used when data does not allow for a complete separation using a hyperplane.

The minimization process gave the parameters for the SVM trainer shown in table 7.2.

subvolume size	**13 x 13 x 13**	**17 x 17 x 17**	**21 x 21 x 21**
RBF sigma	11.1014	7.3312	4.9064
Box constraint	2.9228	3.5326	2.3537

Table 7.2: *Optimal SVM parameters.*

After optimization and training of the SVM, the test data of each subvolume size was classified using a five-fold cross validation and the parameters determined before.

An overview of the complete process can be seen in figure 7.1.

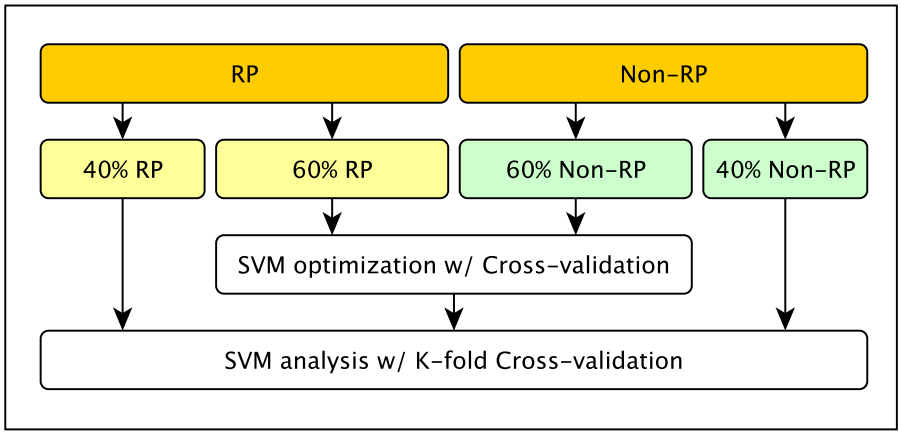

Figure 7.1: *Method utilized to optimize and classify using SVM.*

In the following the results from the classification of each subvolume type is presented. In order to easily compare the output of each different subvolume, an $F_{measure}$ is calculated. The $F_{measure}$ is the harmonic mean of the Sensitivity (S) and Positive Predictive Value (PPV), which is calculated as shown in equation 7.1.

$$F_{measure} = 2\frac{S \cdot PPV}{S + PPV} \tag{7.1}$$

The calculated $F_{measure}$ is between zero and one, with zeros being the worst outcome and one the best.

7.2 Results

The result of the classification is presented in table 7.3.

Subvolume size	**13 x 13 x 13**	**17 x 17 x 17**	**21 x 21 x 21**
Accuracy	59.5%	79.9%	88.7%
Sensitivity	50.6%	76.2%	86.8%
Specificity	86.6%	91.8%	95.8%
Positive predictive value	92.0%	96.8 %	98.8%
Negative predictive value	36.7%	54.1%	64.8%
$F_{measure}$	0.595	0.853	0.924

Table 7.3: *Results of the five-fold cross-validation.*

The outcome of the classification can also be visually confirmed when evaluating sliced versions of randomly sampled subvolumes, as are depicted in figure 7.2-7.10.

7.3 Discussion

The subvolume size of 13x13x13 scored the lowest, while the 17x17x17 subvolumes proved slightly better with a sensitivity of 76.2% and specificity of 91.8%. The best performance was seen when using the 21x21x21 subvolumes which achieved a sensitivity of 86.8% and a specificity of 95.8%. This is also evident judging by the sliced versions of subvolumes classified as true positive (left column) and the slices classified as false negative (right column) present in figure 7.10. The true positive slices clearly contain a more hazy texture, while the false negatives contain small pulmonary vessels. However, when looking at the subvolumes classified as true negative (figure 7.8) and false positive (figure 7.9), it was clear that the classifier needs more diverse training material.

The 17x17x17 subvolumes proves slightly worse as also seen on figure 7.7. Despite the large distinction between the true positive and false positive slices, the amount of true negative and false positive was higher than the 21x21x21 subvolume classification. Again the subvolumes belonging to these categories showed to contain hazy structures, however with a large mixture of pulmonary nodes within.

As seen in figure 7.4, the true positive and false negative slices of 13x13x13 subvolumes both contain hazy areas, making it likely the the subvolume size is simply to small to sample enough features for texture analysis. As with the 17x17x17 and 21x21x21 subvolumes, the true negative and false positive both contain patterns that are reminiscent of pneumonitis, even though the false positives are likely to

be nodule edges from the RP_{neg} subjects.

Based on the results it is evident that the subvolume size of 21x21x21 performed the best, due to its capacity of containing more distinctive textural features.

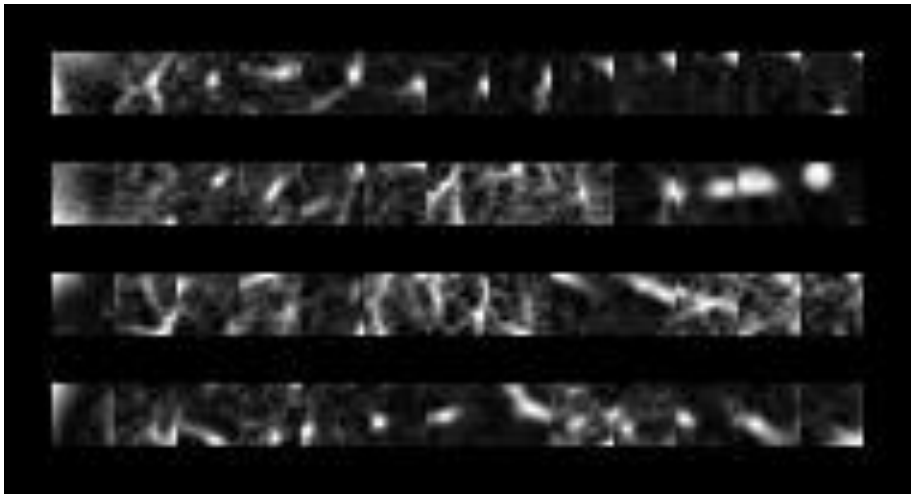

Figure 7.2: *Sliced versions of 13 x 13 x 13 subvolumes that have been classified as true negative.*

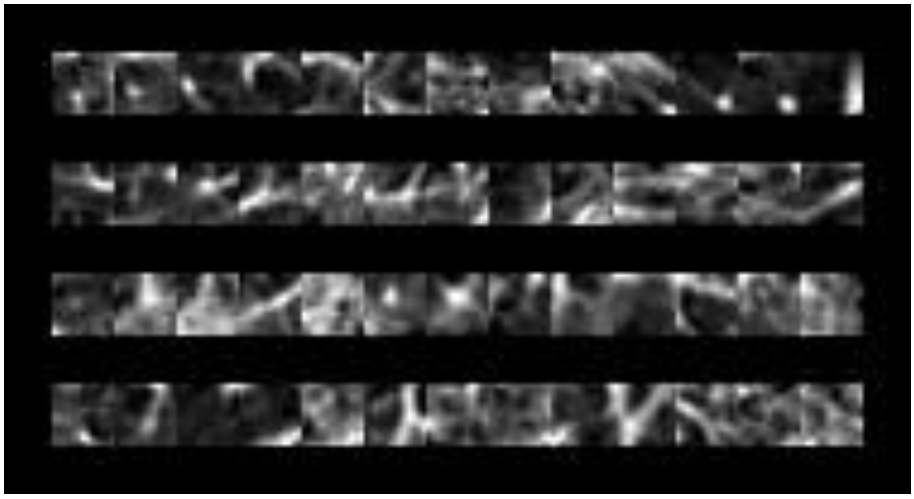

Figure 7.3: *Sliced versions of 13 x 13 x 13 subvolumes that have been classified as false positive.*

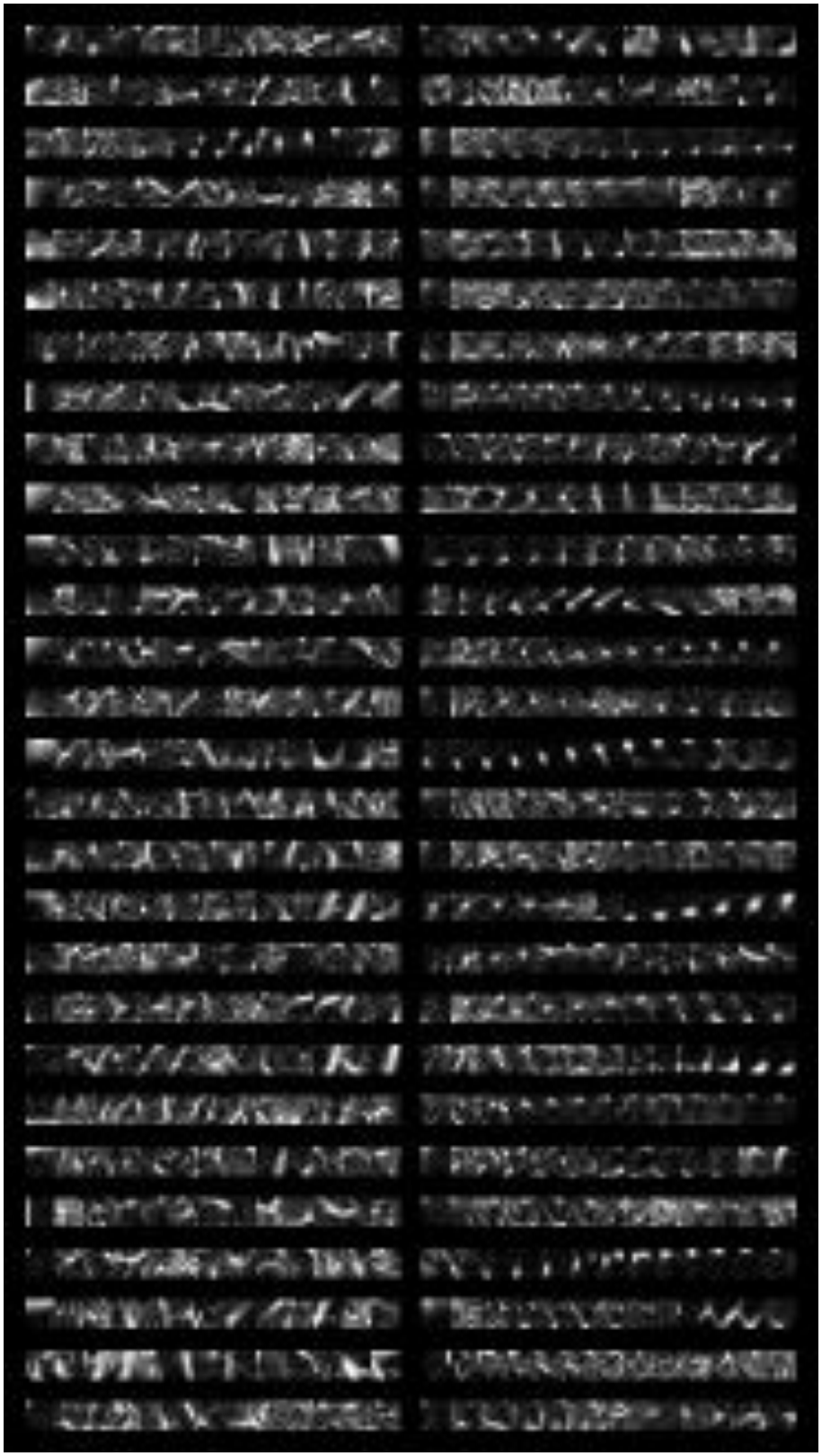

Figure 7.4: *Sliced versions of 13 x 13 x 13 subvolumes selected randomly. Each row contains a sliced subvolume classified as true positive (left column) and a subvolume classified as false negative (right column).*

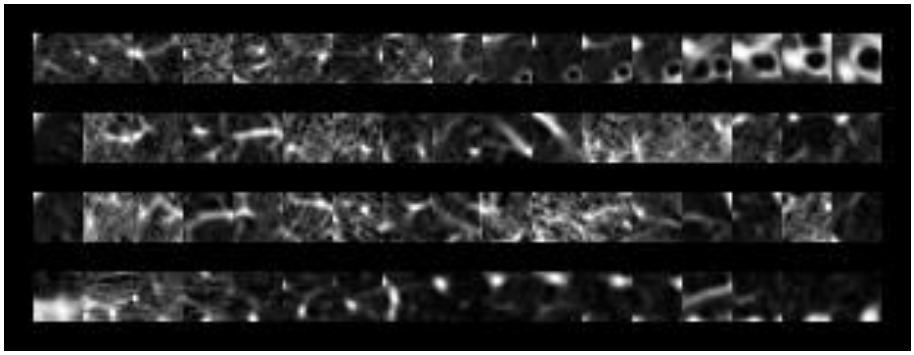

Figure 7.5: *Sliced versions of 17 x 17 x 17 subvolumes that have been classified as true negative.*

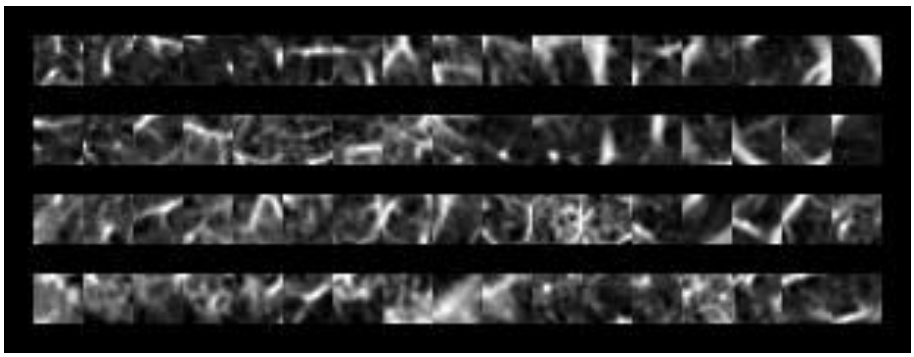

Figure 7.6: *Sliced versions of 17 x 17 x 17 subvolumes that have been classified as false positive.*

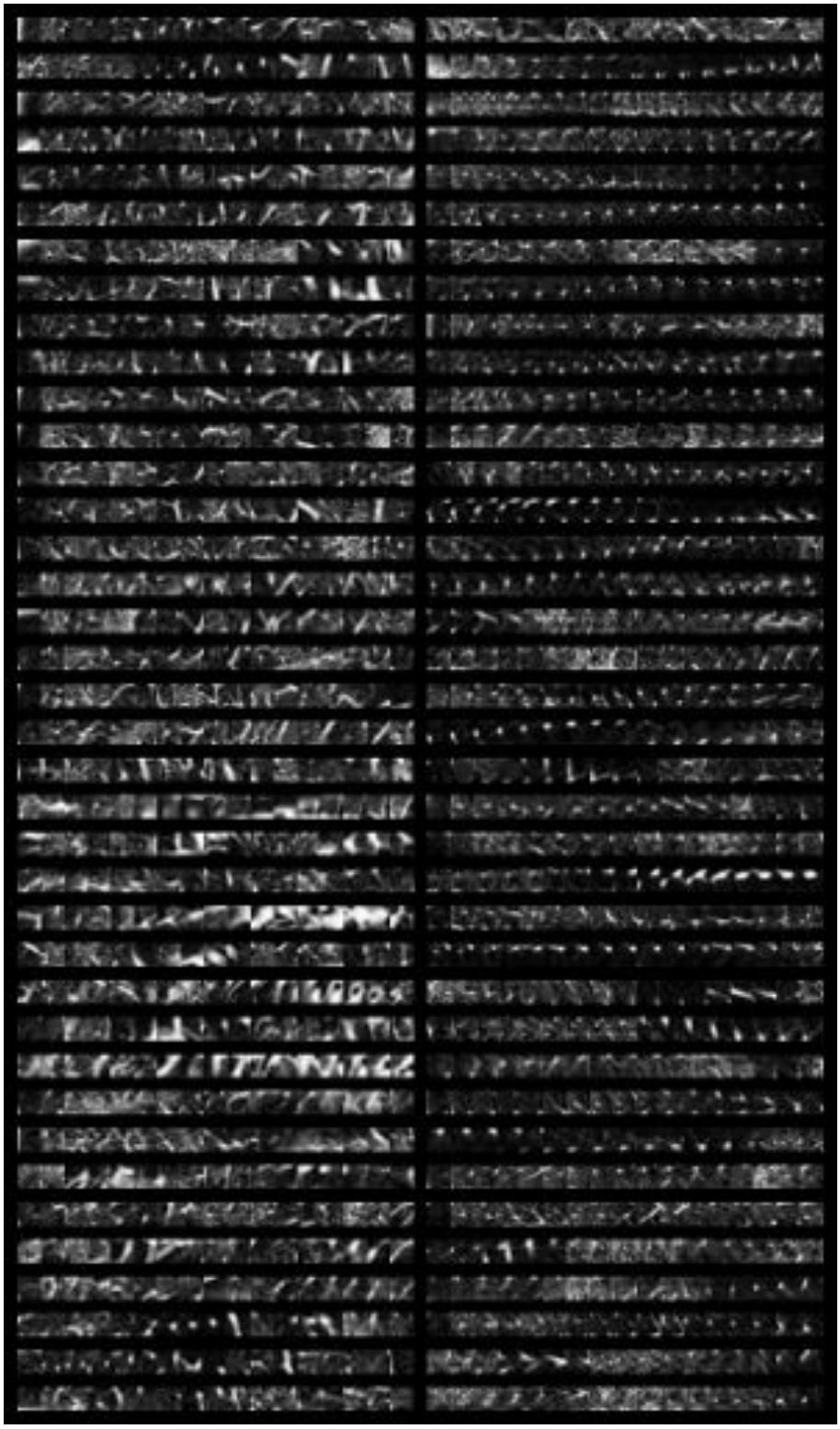

Figure 7.7: *Sliced versions of 17 x 17 x 17 subvolumes selected randomly. Each row contains a sliced subvolume classified as true positive (left column) and a subvolume classified as false negative (right column).*

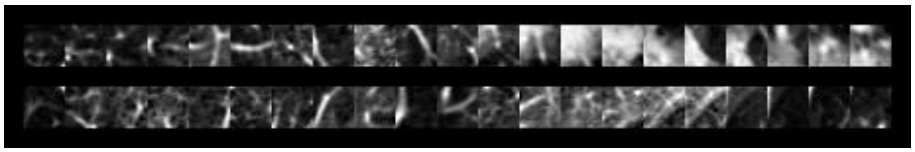

Figure 7.8: *Sliced versions of 21 x 21 x 21 subvolumes that have been classified as true negative.*

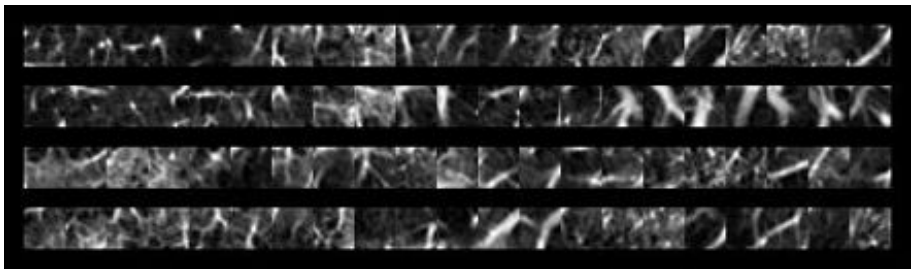

Figure 7.9: *Sliced versions of 21 x 21 x 21 subvolumes that have been classified as false positive.*

Figure 7.10: *Sliced versions of 21 x 21 x 21 subvolumes selected randomly. Each row contains a sliced subvolume classified as true positive (left column) and a subvolume classified as false negative (right column).*

PART IV

Synthesis

CHAPTER 8

Discussion & Conclusion

CAD systems are increasingly relied on for the identification and quantification of lung damage following radiation therapy. The systems use descriptive features to analyze the different textural compositions of the lung parenchyma to classify signs of pneumonitis. However the ability to classify several types of lung damage using the same features and classifier is often difficult, which is also reflected in the results of this work, especially when focusing on pneumonia textures within the false positives and true negatives of the classification. The distinction between treated non-pneumonitis tissue and treated pneumonitis tissue is also made difficult by the fading remains of neoplasms within the treated non-pneumonitis tissue.

As a part of this work, the use of different subvolume sizes was examined, showing that larger volumes provide better classification. However, the increase also reduces the amount of available divisions of the lung, and the divisions will be limited to the central parts of the lungs, missing the occurrences of pneumonitis that are typically found in the boundary regions of the lungs. A tradeoff therefore exists between the desire of having a precise location of damaged tissue and the ability to the detect it within the volume.

With regards to the segmentation of the lungs, it is worth noting that all lung segmentations contain both pulmonary and airway vessels in addition to the parenchyma. This could have been avoided by segmenting the whole airway tree and pulmonary vessel tree and subtracting them from the lung segmentation. However, the relatively large slice thickness made it impossible for the wavefront propagation algorithm to move into smaller lung nodes. Also, the subtraction of non-parenchyma objects would have lead to a significant reduction in the number of subvolumes that could be extracted from within the segmented regions.

A limitation of this study is the classes of which the individual lungs are classified to. An ideal classification would focus on the not only the separation of treated non-pneumonitis tissue and treated pneumonitis tissue, but also between the untreated non-pneumonitis tissue and untreated pneumonitis tissue of the counter lateral lungs. However, the lack of a precise ground truth model and due to the dif-

ferent types of dominating pneumonitis within each subject, it was necessary to limit the field of examination.

Despite the limitations of the study, it was still possible to distinct between treated non-pneumonitis tissue and treated pneumonitis tissue, with an accuracy of 88.7%, when using sub volumes of size 21x21x21.

References

Artaechevarria, X., Pérez-Martín, D., Ceresa, M., Biurrun, G. de, Blanco, D., Montuenga, L. M., et al. (2009). Airway segmentation and analysis for the study of mouse models of lung disease using micro-ct. *Physics in Medicine and Biology*, *54*(22), 7009.

Ataya, S., Elwing, J., Biddinger, P., & Panos, R. J. (2006). Radiation-induced lung injury. *Clinical Pulmonary Medicine*, *13*(4). Available from `http://journals.lww.com/clinpulm/Fulltext/2006/07000/Radiation_Induced_Lung_Injury.3.aspx`

Bagci, U., Bray, M., Caban, J., Yao, J., & Mollura, D. J. (2012, Jan). Computer-assisted detection of infectious lung diseases: a review. *Comput Med Imaging Graph*, *36*(1), 72–84.

Berkey, F. J. (2010, Aug). Managing the adverse effects of radiation therapy. *Am Fam Physician*, *82*(4), 381–388.

Fass, L. (2008, 08). Imaging and cancer: A review. *Molecular oncology*, *2*(2), 115–152. Available from `http://linkinghub.elsevier.com/retrieve/pii/S1574789108000598?showall=true`

Ferlay, J., Shin, H.-R., Bray, F., Forman, D., Mathers, C., & Parkin, D. M. (2010, Jun). Estimates of worldwide burden of cancer in 2008: Globocan 2008. *Int J Cancer*.

Gangeh, M. J., Sørensen, L., Shaker, S. B., Kamel, M. S., & Bruijne, M. de. (2011). Multiple classifier systems in texton-based approach for the classification of ct images of lung. In *Proceedings of the 2010 international miccai conference on medical computer vision: recognition techniques and applications in medical imaging* (pp. 153–163). Berlin, Heidelberg: Springer-Verlag. Available from `http://dl.acm.org/citation.cfm?id=1964478.1964497`

Kocak, Z., Evans, E. S., Zhou, S.-M., Miller, K. L., Folz, R. J., Shafman, T. D., et al. (2005, Jul). Challenges in defining radiation pneumonitis in patients with lung cancer. *Int J Radiat Oncol Biol Phys*, *62*(3), 635-8.

Lim, E., Baldwin, D., Beckles, M., Duffy, J., Entwisle, J., Faivre-Finn, C., et al. (2010, Oct). Guidelines on the radical management of patients with lung cancer. *Thorax*, *65 Suppl 3*, iii1-27.

Lim, J., Kim, N., Seo, J. B., Lee, Y. K., Lee, Y., & Kang, S.-H. (2011, Dec). Regional context-sensitive support vector machine classifier to improve automated identification of regional patterns of diffuse interstitial lung disease. *J Digit Imaging*, *24*(6), 1133-40.

Marks, L. B., Yu, X., Vujaskovic, Z., Jr, W. S., Folz, R., & Anscher, M. S. (2003). Radiation-induced lung injury. *Seminars in Radiation Oncology*, *13*(3), 333 - 345. Available from http://www.sciencedirect.com/science/article/pii/S1053429603000341

Mehta, V. (2005, Sep). Radiation pneumonitis and pulmonary fibrosis in non-small-cell lung cancer: pulmonary function, prediction, and prevention. *Int J Radiat Oncol Biol Phys*, *63*(1), 5-24.

Palma, D. A., Koste, J. R. van Sörnsen de, Verbakel, W. F. A. R., & Senan, S. (2011, May). A new approach to quantifying lung damage after stereotactic body radiation therapy. *Acta Oncol*, *50*(4), 509-17.

Park, S. C., Tan, J., Wang, X., Lederman, D., Leader, J. K., Kim, S. H., et al. (2011, Feb). Computer-aided detection of early interstitial lung diseases using low-dose ct images. *Phys Med Biol*, *56*(4), 1139–1153.

Provatopoulou, X., Athanasiou, E., & Gounaris, A. (2008). Predictive markers of radiation pneumonitis. *Anticancer Res*, *28*(4C), 2421-32.

Rodrigues, G., Lock, M., D'Souza, D., Yu, E., & Van Dyk, J. (2004, May). Prediction of radiation pneumonitis by dose - volume histogram parameters in lung cancer–a systematic review. *Radiother Oncol*, *71*(2), 127-38.

Rovirosa, A., & Valduvieco, I. (2010). Radiation pneumonitis. *Clinical Pulmonary Medicine*, *17*(5). Available from http://journals.lww.com/clinpulm/Fulltext/2010/09000/Radiation_Pneumonitis.3.aspx

Sebastian, B., Unnikrishnan, A., & Balakrishnan, K. (2012, April). Grey level co-occurrence matrices: Generalisation and some new features. *nternational Journal of Computer Science, Engineering and Information Technology (IJCSEIT)*, *2*(2), 151-157.

Shiraishi, J., Li, Q., Appelbaum, D., & Doi, K. (2011, Nov). Computer-aided diagnosis and artificial intelligence in clinical imaging. *Semin Nucl Med*, *41*(6), 449-62.

Siegel, R., Naishadham, D., & Jemal, A. (2012). Cancer statistics, 2012. *CA Cancer J Clin*, *62*(1), 10-29.

Tolouee, A., Moghaddam, H. A., Forouzanfar, M., Gity, M., & Garnavi, R. (2011). Image based diagnostic aid system for interstitial lung diseases. *Expert Systems with Applications*, *38*(6), 7755 - 7765. Available from http://www.sciencedirect.com/science/article/pii/S095741741001496X

Yirmibesoglu, E., Higginson, D. S., Fayda, M., Rivera, M. P., Halle, J., Rosenman, J., et al. (2012, Jan). Challenges scoring radiation pneumonitis in patients irradiated for lung cancer. *Lung Cancer*.

Zhu, Y., Tan, Y., Hua, Y., Zhang, G., & Zhang, J. (2011, Nov). Automatic segmentation of ground-glass opacities in lung ct images by using markov random field-based algorithms. *J Digit Imaging*.

Appendix

APPENDIX A

Literature search

Background

A systemized literature search was performed in order to obtain background material on the subject of radiation-induced lung disease. Figure A.1 illustrates the initial areas of investigation.

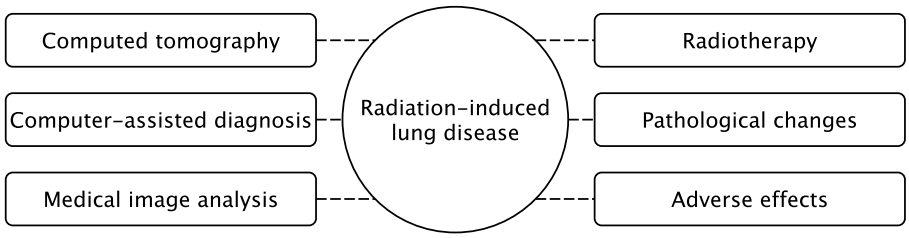

Figure A.1: *Initial areas of investigation around the subject of radiation-induced lung disease.*

Information sources

The two databases, PubMed and Embase, were chosen for their wast library of publications within health sciences. PubMed is well known as the most largest and up-to-date database, while Embase indexes a lot of additional journals (mainly european), which are not covered by PubMed.

Search strategy

Each database has a thesaurus (subject index), which were first searched using the following keywords generated based on the initial areas of investigation shown above.

- Radiotherapy
- Lung damage
- Interstitial lung disease
- Radiation damage
- Computed tomography
- Radiation-induced lung disease
- Radiation pneumonitis and fibrosis
- Lung segmentation
- Computer-assisted diagnosis
- Medical image analysis

Using the keywords, a list of MeSH (Medical Subject Headings) for PubMed and Emtree terms for Embase, was generated and combined

as shown in Table A.1. Additional free text search terms were also used during the search, if no matching MeSH or Emtree terms could be found. Following the primary search, all literature was examined using the snowball method in which the references of the before mentioned publications are examined and acquired if found relevant.

Exclusion criteria

Publications older than the year of 1992 were excluded in the primary search phase, based on the assumption that the publications would be outdated with regards to modern medical image analysis.

During the search of Embase, the results were filtered to only contain publications within Embase in order to avoid overlapping from the Medline (PubMed) database.

Inclusion criteria

Only peer-reviewed publications, reviews and clinical trials were included. Additionally, publications older than the year of 1992 were included if referenced within relevant publications found during the primary search phase.

Results

A total of 204 publications were found relevant during the primary database search, and an additional 40 were found using the snowball method. The distribution of publications across time as well as type of publication can be seen in Figure A.2.

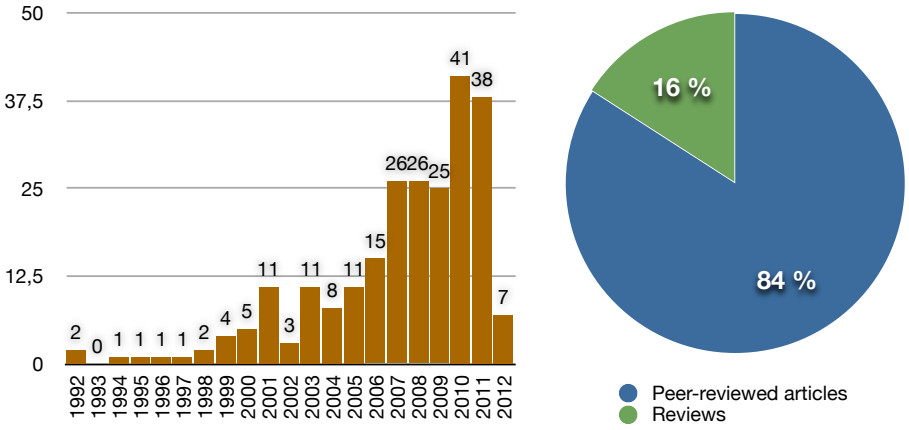

Figure A.2: *Resulting publications sorted by both year and type.*

As depicted, the literature found through the search was predominantly from within the last 10 years and mainly consisted of peer-reviewed articles.

Database	Search term	Type	Combinations	Additional filters	Publications		
					Abstracts	Relevant	Total hits
PubMed	**A** radiation injuries	MeSH term	A *and* G	None	39	16	181
	B radiation pneumonitis	MeSH term	A *and* B	None	31	21	170
	C diagnosis, computer-assisted	MeSH term	C *and* F	None	76	51	574
	D radiation-induced lung disease	Free text	None	None	23	18	271
	E lung injury	MeSH term	Not searched	None	-	-	-
	F lung	Free text	Not searched	None	-	-	-
	G segmentation	Free text	G *and* F	None	33	28	69
	H pneumonitis	Mesh Term	H *and* C	None	9	5	40
Embase	**A** radiation injury	Emtree term	A *and* (D *or* F)	B, C, E , G, H, I, J	45	22	352
	B radiation pneumonia	Emtree term	None	A, C, D, G, K	87	38	997
	C pneumonia	Emtree term	Not searched	None	-	-	-
	D lung injury	Emtree term	Not searched	None	-	-	-
	E lung fibrosis	Emtree term	Not searched	None	-	-	-
	F lung disease	Emtree term	Not searched	None	-	-	-
	G lung cancer	Emtree term	Not searched	None	-	-	-
	H lung toxicity	Emtree term	Not searched	None	-	-	-
	I inflammation	Emtree term	Not searched	None	-	-	-
	J tissue injury	Emtree term	Not searched	None	-	-	-
	K side effects	Emtree term	Not searched	None	-	-	-
	L epidemiology	Emtree term	L *and* G	None	16	5	201
					359	204	2855

Table A.1: *A breakdown of the databases searched and the type and combinations of search terms used to find relevant publications.*